Author Contributions:
Conceptualization: Yi An, Huaning Wang, Qingquan Liu, Xiaoliang Wang
Data curation: Can Huang, Chao Hu
Formal analysis: Chao Hu, Chun Feng
Funding acquisition: Chun Feng, Huaning Wang, Qingquan Liu, Xiaoliang Wang
Investigation: Can Huang, Xiaoliang Wang
Methodology: Chao Hu, Yi An, Chuanqi Shi, Chun Feng, Huaning Wang
Project Administration: Qingquan Liu
Software: Can Huang, Chuanqi Shi, Xiaoliang Wang
Supervision: Huaning Wang, Qingquan Liu, Xiaoliang Wang
Validation: Can Huang
Writing – original draft: Can Huang
Writing – review & editing: Qingquan Liu, Xiaoliang Wang

Numerical Simulation of the Large-Scale Huangtian (China) Landslide-Generated Impulse Waves by a GPU-Accelerated Three-Dimensional Soil–Water Coupled SPH Model

Can Huang[1], Chao Hu[1], Yi An[2] , Chuanqi Shi[2], Chun Feng[2], Huaning Wang[3], Qingquan Liu[1] , and Xiaoliang Wang[1]

[1]Department of Mechanics, School of Aerospace Engineering, Beijing Institute of Technology, Beijing, China, [2]Institute of Mechanics, Chinese Academy of Sciences, Beijing, China, [3]School of Aerospace Engineering and Applied Mechanics, Tongji University, Shanghai, China

Abstract This work presents an improved soil–water coupling model to simulate landslide-generated impulse waves (LGIWs) in a unified smoothed particle hydrodynamics (SPH) framework, where both water flow and landslide motions are modeled by SPH using an interface coupling technique. Graphics processing unit technology based on an open-source platform DualSPHysics is chosen to employ the landslide dynamics and soil–water interface coupling to achieve the capability of large-scale simulation and high-resolution modeling for three-dimensional LGIW problems. A subaerial landslide-generated water waves, is simulated to demonstrate the accuracy and ability of this model. The Huangtian LGIW is then simulated to reproduce the entire disaster chain, including landslide dynamics, fluid–solid interaction, and surge wave generation. Particle resolution dependence is examined, giving a particle distance of 5.0 m, which can provide a converged landslide deposit and surge wave. The simulation shows that in the Huangtian LGIW, the landslide deposit volume was approximately 41.6 million m^3 (600 m width, 768 m length, and 400 m above the still water level), with an immersed landslide volume of 11.3 million m^3; for the surge wave, the maximum wave and run-up heights were 34.3 and 48 m, respectively. These results are within the estimated ranges of both the landslide and surge wave according to limited field survey data. The case study of the Huangtian LGIW provides a typical reference of how to reproduce a reliable whole process of large scale multi-physical and multiscale LGIW, including full information of landslide dynamics, interface coupling behavior, and surge wave characteristics.

Plain Language Summary We developed a graphics processing unit accelerated soil-water coupled smoothed particle hydrodynamics solver to simulate very large-scale landslide generated impulse waves (LGIW). Taking Huangtian LGIW as an example, the validity of the present solver is shown to provide full information of both landslides and impulse waves which are comparable with field data, which could be helpful for large scale LGIW assessments.

1. Introduction

Large-scale landslides near restricted water bodies, such as lakes, dammed reservoirs, and mountain rivers, may generate huge surge waves that in turn cause casualties and building damage. For example, a catastrophic rock-slide, with a large volume of approximately 3×10^8 m^3, slipped and fell into the Vajont reservoir in Italy in 1963. The resultant surge wave overtopped the Vajont dam causing the death of nearly two thousand people (Panizzo et al., 2005). This type of disaster chain involves complex multi-physical and multiscale problems, including landslide deformation, free-surface capture, multiphase coupling, and strong three-dimensional (3D) structural evolution.

Numerous experimental studies have been conducted using indoor water channels. Generally, according to the type of sliding mass, these studies can be divided into two categories such as rigid-body models (Ataie-Ashtiani & Najafi-Jilani, 2008; Heller & Spinneken, 2015; Risio & Sammarco, 2008) and deformed-body models (Fritz et al., 2001, 2004; McFall et al., 2018; Mohammed & Fritz, 2012). Heller and Spinneken (2013) reported a variation in maximum wave amplitude and height in the three important block model parameters under the two-dimensional (2D) condition. Heller et al. (2016) conducted a multitude of 3D physical model tests. Deformed-body usually uses granular material composed of some gravels. Researchers in this field have carried out a large number of studies on landslide generated impulse waves (LGIWs) considering the Froude number,

relative volume, and thickness (Fritz et al., 2001, 2004; McFall et al., 2018; McFall & Fritz, 2017; Mohammed & Fritz, 2012). Physical model tests can help to understand the movement or deformation of landslides, and the generation and propagation of surge waves. However, there are clear differences between laboratory scale and real-world LGIWs, and physical model tests are complex and expensive. Numerical technology has become an effective method to carry out abundant model tests and perform real-world LGIW simulations.

Among the many potential numerical methods, the mesh-free method, smoothed particle hydrodynamics (SPH), is widely used for water flows with large surface deformation (Yang et al., 2014; Zheng et al., 2009) and large deformation simulations in granular flow (An et al., 2016; W. Chen & Qiu, 2012; Huang & Liu, 2020; Minatti & Paris, 2015; Peng et al., 2015). Over the years, SPH has also been widely used in simulating soil failure deformation, granular media flow, and soil-water coupling. Several studies have employed the elasto-plastic SPH model to analyze slope stability and corresponding slope failure simulations, as presented by Bui et al. (2011) and Nonoyama et al. (2015). Additionally, Peng et al. (2016) proposed a unified numerical framework for granular modeling by combining a hypoplastic model and a Bagnold-type rheology relation. C. Wang et al. (2016) developed a two-phase SPH mixture model to simulate water-soil interactions, which demonstrated its applicability in simulating single-phase flows and solving the problem of soil excavation by high-velocity water jets. Zhang et al. (2016, 2019) proposed and validated a two-phase coupled SPH model through the simulation of a dike failure test and conducting stability analysis of a soil slope. Feng et al. (2022) presented a new fully-coupled SPH formulation for unsaturated soils, which investigates the influence of rainfall infiltration on slope stability and allows for the simulation of both triggering and post-failure mechanisms. These studies demonstrate the usefulness and efficiency of SPH in geotechnical and geological engineering applications, and highlight its ability to simulate a range of phenomena including slope stability, rainfall infiltration, and post-failure mechanisms.

In LGIW simulations using the SPH method, the water flow is usually modeled using Navier–Stokes equations, while descriptions of the sliding mass usually take two different forms. Similar to physical tests, the sliding mass can be divided into two types: rigid-body and deformable-body. Clearly, compared with rigid bodies, deformable bodies are advantageous in describing the flow characteristics of sliding masses and their coupling with water waves. Deformation behavior is usually modeled using the discrete element method (DEM), non-Newtonian flow model, or elastoplastic constitutive model. The movement of a sliding mass can be directly described by the interaction between DEM particles. For instances, Tan and Chen (2017) adopted drag force and buoyancy for solid–fluid interaction; Bu et al. (2022) considered the linear Darcy's law in their SPH–DEM coupling. They provided numerical results from several benchmark experimental cases, proving that the DEM can successfully represent the deformation of a landslide mass. However, the DEM method for the soil phase usually involves the calibration of many parameters (X. Wang et al., 2019; X. Wang & Li, 2014). The non-Newtonian flow model adopts Navier–Stokes equations to describe the movement of soil and water in a unified SPH framework, which can be easily implemented algorithmically. The usual treatment method is to obtain the viscosity of the soil through the shear rate and a yield criterion, such as the Mohr–Coulomb criterion, and then substitute this into the momentum equation. Some studies, using revised non-Newtonian models (Krimi et al., 2018; Xenakis et al., 2017; Yeylaghi et al., 2017), have provided verifications for indoor physical model tests. Compared with a rigid model, the non-Newtonian model can better reflect the flow characteristics of soil, but a comprehensive description of the structural failure of a landslide mass requires an elastoplastic model. Shi et al. (2016) and X. Wang et al. (2021) adopted the Drucker–Prager constitutive model with a non-associated flow rule in SPH formulations to model LGIWs within a continuum framework. This constitutive model has been used to simulate granular failure and flow problems (An et al., 2016; Bui et al., 2008; W. Chen & Qiu, 2012; Huang et al., 2022), and it can successfully replicate the elastoplastic behavior of particle flow. To reproduce the occurrence process of a LGIW disaster chain, the elastoplastic constitutive model can better describe the slope stability, large deformation, and granular flow, compared with other model types (Bui et al., 2011; Peng et al., 2021; Zhang et al., 2018; Zhu et al., 2018).

Current research mainly focuses on the establishment of a two-phase model and validation of indoor scaled problems. A possible reason limiting large-scale LGIW simulation is computing efficiency. Huang et al. (2022) pointed out that the number of particles in many studies is relatively small, limiting their applicability to large-scale geological problems. Recently, graphics processing unit (GPU) technology has been shown to greatly improve computing efficiency in many studies in the field of SPH simulation (J. Y. Chen et al., 2020; Crespo et al., 2015; Zhan et al., 2019). For real-world large-scale LGIW cases, Shi et al. (2015) and Vacondio et al. (2013) mainly considered the landslide as a rigid body with an initial specified estimated velocity. Their research was mainly concerned with the movement of water flow, simplifying the movement of the landslide, and being unable to

reflect the deformation and flow processes of a real landslide. However, it is important for LGIW studies to consider the deformation of the landslide, because this deformation significantly affects the movement of water flow (Shi et al., 2016). Xu (2020) simulated the Vajont LGIW using the SPH–DEM coupling model, in which the sliding mass was represented by DEM particles. The aforementioned studies all employed GPU acceleration technology to run simulations. Therefore, a GPU acceleration algorithm is essential to simulate real-world large-scale LGIW problems.

In addition, to the best of our knowledge, convergence analysis of 3D LGIW involving complex multi-physical and multiscale problems has never previously been reported in the framework of SPH method. Convergence analysis of single phase landslides with the elastoplastic SPH model has recently been reported (Huang et al., 2022; Peng et al., 2021). For more complex soil–water interface coupling processes, it is necessary to discuss the convergence of numerical simulations, which helps find a suitable particle distance and avoids wasting computing resources without compromising accuracy for large-scale physical problems. The necessary condition for convergence analysis is an improvement in calculation efficiency, such as that brought by the GPU parallel algorithm.

In previous studies (Shi et al., 2016; X. Wang et al., 2021), it was found that water will sometimes penetrate into the soil at the soil–water interface which may cause computational problems. Therefore, the interface treatment must be further improved to adapt to large-scale LGIW simulations.

In summary, this work aims to improve the computation efficiency and accuracy of our previously presented coupled SPH model (Shi et al., 2016; X. Wang et al., 2021); this will enhance its ability to simulate large-scale practical situations with soil–water coupling effects. The remainder of this paper consists of four sections. The numerical model for soil–water coupling processes, mainly including an improved interface treatment, is described in Section 2. In Section 3, an indoor scaled LGIW example is presented to validate the model. In Section 4, a practical case, the Huangtian LGIW, is analyzed in detail in terms of convergence and the generation and propagation of a surge wave. Finally, our conclusions are summarized in Section 5.

2. Numerical Model

2.1. Models for Water and Soil

The governing equations of water are the mass conservation and momentum conservation equations, which are discretized in the SPH method as follows:

$$\frac{d\rho_i}{dt} = \sum_{j=1}^{N} m_j (v_i^\alpha - v_j^\alpha) \frac{\partial W_{ij}}{\partial x_i^\alpha} \tag{1}$$

$$\frac{dv_i^\alpha}{dt} = -\sum_{j=1}^{N} m_j \left(\frac{p_i}{\rho_i^2} + \frac{p_j}{\rho_j^2} + \prod_{ij} \right) \frac{\partial W_{ij}}{\partial x_i^\alpha} + g^\alpha \tag{2}$$

where superscript α represents the Cartesian space coordinates x, y, z; i and j are two water particles and N is the number of neighbor particles for particle i; m, ρ and v denote the mass, density, and velocity of water, respectively; g^α is a body force and herein refers to the acceleration of gravity; the kernel function W_{ij} is used herein as a cubic spline function:

$$W(r_{ij}, h) = \alpha_D \begin{cases} \frac{3}{4}q^3 - \frac{3}{2}q^2 + 1, & 0 \le q < 1 \\ \frac{1}{4}(2-q)^3, & 1 \le q < 2, \ q = \frac{r_{ij}}{h} \\ 0, & q \ge 2 \end{cases} \tag{3}$$

where r_{ij} is the distance between particles i and j, and h is the smoothing length.

Weak compressible treatment is used in the continuity equation, and pressure p_i is calculated by the equation of state (Monaghan, 2005):

$$p_i = \frac{c^2 \rho_0}{\gamma} \left(\left(\frac{\rho_i}{\rho_0} \right)^\gamma - 1 \right) \tag{4}$$

where $\gamma = 7$, reference density of water $\rho_0 = 1,000$ kg/m³, and numerical speed of sound c is set to 10 times the maximum water velocity to maintain the density variation within 1%.

Π_{ij} is an artificial viscous term used to suppress numerical fluctuation (Monaghan, 2005), which is written as:

$$\Pi_{ij} = \begin{cases} \dfrac{-\alpha \bar{c}_{ij} \mu_{ij}}{\bar{\rho}_{ij}}, & \boldsymbol{v}_{ij} \cdot \boldsymbol{r}_{ij} < 0 \\[4mm] 0, & \boldsymbol{v}_{ij} \cdot \boldsymbol{r}_{ij} \geq 0 \end{cases} \tag{5}$$

where $\mu_{ij} = h\boldsymbol{v}_{ij} \cdot \boldsymbol{r}_{ij} / \left(r_{ij}^2 + 0.01h^2 \right)$, $\bar{\rho}_{ij} = (\rho_i + \rho_j)/2$, $\bar{c}_{ij} = (c_i + c_j)/2$, $\boldsymbol{v}_{ij} = \boldsymbol{v}_i - \boldsymbol{v}_j$, and $\boldsymbol{r}_{ij} = \boldsymbol{r}_i - \boldsymbol{r}_j$; α is a viscous constant with a value between 0 and 1, and herein $\alpha = 0.05$ for water, $\alpha = 0.1$ for soil.

An elastoplastic soil model within the framework of the SPH method has been established previously (An et al., 2016; Bui et al., 2008). The discrete mass conservation and momentum conservation equations for soil are expressed as:

$$\frac{d\rho_i}{dt} = \sum_{j=1}^{N} m_j (v_i^\alpha - v_j^\alpha) \frac{\partial W_{ij}}{\partial x_i^\alpha} \tag{6}$$

$$\frac{dv_i^\alpha}{dt} = \sum_{j=1}^{N} m_j \left(\frac{\sigma_i^{\alpha\beta} + \sigma_j^{\alpha\beta}}{\rho_i \rho_j} - \prod_{ij} \delta^{\alpha\beta} + F_{ij}^n R_{ij}^{\alpha\beta} \right) \frac{\partial W_{ij}}{\partial x_i^\beta} + g^\alpha \tag{7}$$

where superscripts α and β represent the Cartesian space coordinates x, y, z and satisfy Einstein's summation convention. The artificial stress term $F_{ij}^n R_{ij}^{\alpha\beta}$ acts to reduce the tension instability caused by stretching, where $F_{ij} = W_{ij}/W(\Delta x, h)$. The index $n = 2.55$, and $R_{ij}^{\alpha\beta} = R_i^{\alpha\beta} + R_j^{\alpha\beta}$, where $R_i^{\alpha\beta}$ and $R_j^{\alpha\beta}$ are the components of the artificial stress tensor at particle i and j respectively. The total stress tensor $\sigma^{\alpha\beta}$ can be obtained using the constitutive equation expressed in the rate form:

$$\frac{d\sigma_i^{\alpha\beta}}{dt} = \sigma_i^{\alpha\gamma} \dot{\omega}_i^{\beta\gamma} + \sigma_i^{\gamma\beta} \dot{\omega}_i^{\alpha\gamma} + 2G\dot{e}_i^{\alpha\beta} + K\dot{\varepsilon}_i^{\gamma\gamma} \delta_i^{\alpha\beta} - \dot{\lambda}_i \left[3\alpha_\psi K \delta^{\alpha\beta} + \frac{G}{\sqrt{J_2}} s_i^{\alpha\beta} \right] \tag{8}$$

where $s^{\alpha\beta}$ is the deviatoric stress tensor. $\delta^{\alpha\beta}$ is Kronecker's delta function; $\delta^{\alpha\beta} = 1$ if $\alpha = \beta$, and $\delta^{\alpha\beta} = 0$ if $\alpha \neq \beta$. $\dot{\varepsilon}^{\gamma\gamma}$ refers to the sum of the three principal strain rates. K and G are the elastic bulk modulus and shear modulus, which relate to Young's modulus E and Poisson's ratio v, respectively. The rate of change of the plastic multiplier $\dot{\lambda}$ influences the plastic strain and can be calculated as follows (An et al., 2016; Bui et al., 2008):

$$\dot{\lambda}_i = \begin{cases} \dfrac{3\alpha_\varphi K \dot{\varepsilon}_i^{\gamma\gamma} + \left(G/\sqrt{J_2} \right) s_i^{\alpha\beta} \dot{\varepsilon}_i^{\alpha\beta}}{9\alpha_\varphi \alpha_\psi K + G}, & f(I_1, J_2) = 0 \\[4mm] 0, & f(I_1, J_2) < 0 \end{cases} \tag{9}$$

where $f(I_1, J_2)$ denotes the Drucker–Prager yield function relating to cohesion c and internal friction angle φ; α_φ and α_ψ are constants related to the friction angle φ and dilatancy angle ψ, respectively. The strain rate tensor $\dot{\varepsilon}^{\alpha\beta}$ and spin rate tensor $\dot{\omega}^{\alpha\beta}$ used to calculate the stress rate tensor can be discretized as follows:

$$\dot{\varepsilon}^{\alpha\beta} = \frac{1}{2} \left[\sum_{j=1}^{N} \frac{m_j}{\rho_j} (v_j^\alpha - v_i^\alpha) \frac{\partial W_{ij}}{\partial x_i^\beta} + \sum_{j=1}^{N} \frac{m_j}{\rho_j} \left(v_j^\beta - v_i^\beta \right) \frac{\partial W_{ij}}{\partial x_i^\alpha} \right] \tag{10}$$

$$\dot{\omega}^{\alpha\beta} = \frac{1}{2} \left[\sum_{j=1}^{N} \frac{m_j}{\rho_j} (v_j^\alpha - v_i^\alpha) \frac{\partial W_{ij}}{\partial x_i^\beta} - \sum_{j=1}^{N} \frac{m_j}{\rho_j} \left(v_j^\beta - v_i^\beta \right) \frac{\partial W_{ij}}{\partial x_i^\alpha} \right] \tag{11}$$

2.2. Soil–Water Coupling Method

This study primarily improves the treatment of soil–water interface, including the soil–water interaction and the addition of a repulsive force, in comparison to the previous model (Shi et al., 2016; X. Wang et al., 2021). The

permeability coefficient of common soils, ranging from clay to gravel, is in the order of 10^{-10}–10^{-1} m/s. The low permeability coefficient causes the permeation time to be much larger than the time it takes for a landslide to move from start to stop, which is usually within seconds to several minutes, thus the seepage can be neglected. Especially, for soil mass with a high permeability coefficient, such as gravel and glass beads, the permeation time is short enough to be not negligible, and mixing should be taken into consideration. Under this circumstance, the predefined bulk density is often applied to represent this mixture, which can be found in some previous LGIW studies using multiphase non-Newton fluid model (Krimi et al., 2018; Mahallem et al., 2022). Therefore, in this work, we ignored the seepage or mixing process for low permeability coefficient material, while used predefined bulk density for high permeability coefficient material, and then only consider the interface interaction process. Shao (2012) emphasized that for multi-fluid systems, the stress and deformation should be consistent at the interface, allowing the soil–water interface to be considered a moving and deforming boundary in this study. The interface interaction between soil and water is mainly considered by decoupling the soil and water phases.

Following the implementation of the wall boundary condition of Adami et al. (2012) and fluid–structure interaction (Han & Hu, 2018) for each interacting particle pair (w, s) (representing the water and soil particles, respectively), we can approximate the imagining density ρ_s^d and velocity $\boldsymbol{v}_s^d$ on soil particle s using:

$$\rho_s^d = \frac{\sum_w m_w W_{sw}}{\sum_w \frac{m_w}{\rho_w} W_{sw}} \tag{12}$$

$$\boldsymbol{v}_s^d = 2\boldsymbol{v}_s - \boldsymbol{v}_w \tag{13}$$

Furthermore, the imaging pressure p_s^d can be calculated using Equation 4. The contribution of soil particle s to water particle w in the continuity and momentum equations is written as:

$$\frac{d\rho_w}{dt} = m_w\left(v_w{}^\alpha - v_s^{d\,\alpha}\right)\frac{\partial W_{ws}}{\partial x_w{}^\alpha} \tag{14}$$

$$\frac{dv_w^\alpha}{dt} = -m_w\left(\frac{p_w}{\rho_w^2} + \frac{p_s^d}{\left(\rho_s^d\right)^2} + \prod_{ws}\right)\frac{\partial W_{ws}}{\partial x_w{}^\alpha} \tag{15}$$

Similarly, the contribution of water particle w to soil particle s is calculated by:

$$\frac{d\rho_s}{dt} = m_s\left(v_s{}^\alpha - v_w^{d\,\alpha}\right)\frac{\partial W_{sw}}{\partial x_s{}^\alpha} \tag{16}$$

$$\frac{dv_s^\alpha}{dt} = \frac{m_w{}^2}{m_s}\left(\frac{p_w}{\rho_w^2} + \frac{p_s^d}{\left(\rho_s^d\right)^2} + \prod_{ws}\right)\frac{\partial W_{sw}}{\partial x_s{}^\alpha} \tag{17}$$

where Equation 17 is obtained according to Newton's third law of motion.

A soft, distance-dependent, pairwise repulsive force is applied along the centerline of the neighboring pairs of water and soil particles to prevent them from penetrating each other. The repulsive force expression (M. Liu et al., 2012) is written as:

$$\boldsymbol{F}_{ij} = 0.01c^2 \cdot A \cdot f(\eta) \cdot \frac{\boldsymbol{x}_{ij}}{r_{ij}{}^2} \tag{18}$$

$$A = \begin{cases} 1 - r_{ij}/\Delta d, & 0 < r_{ij} < \Delta d \\ 0, \text{otherwise} \end{cases}, \eta = r_{ij}/(0.5h) \tag{19}$$

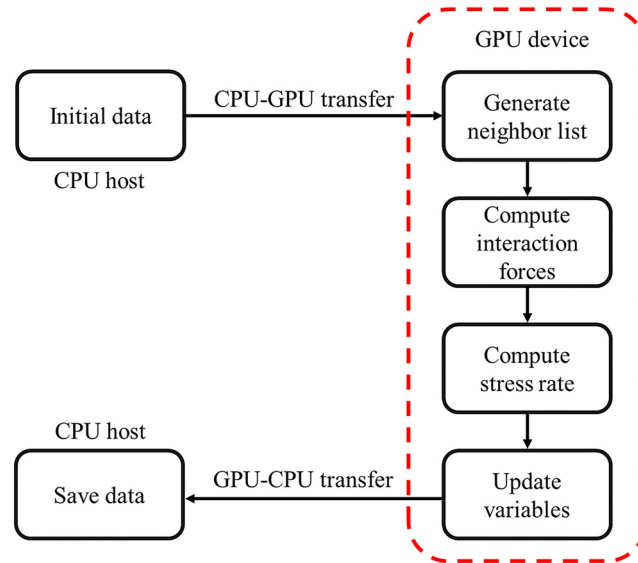**Figure 1.** Flowchart of the simulation process in our program.

$$f(\eta) = \begin{cases} 2/3, & 0 < \eta \le 2/3 \\ 2\eta - 1.5\eta^2, & 2/3 < \eta < 1 \\ 0.5(2-\eta)^2, & 1 < \eta \le 2 \\ 0, & \eta > 2 \end{cases} \tag{20}$$

where Δd is the initial particle distance. This soft repulsive force model can prevent unphysical particle penetration without obvious pressure oscillation. The above treatment for the soil–water interface is also applied to the fluid boundary and soil boundary.

2.3. Implementation and GPU Acceleration

We adopted the explicit Verlert scheme for the time integration of the above-mentioned discretization. The time step depends on the Courant–Friedrichs–Lewy (CFL) conditions, external force, and viscous dissipation. The following expression of the variable time step proposed by Monaghan and Kos (1999) was applied:

$$\Delta t_f = \min\left(\sqrt{\frac{h}{|f_a|}}\right), \Delta t_{cv} = \min_a\left(\frac{h}{c_s + \max_b\left(h v^{ab} r^{ab}/r_{ab}^2\right)}\right) \tag{21}$$

$$\Delta t = N_{CFL} \cdot \min(\Delta t_f, \Delta t_{cv})$$

where the CFL number N_{CFL} is 0.2, and f_a is the per unit mass force.

In 3D SPH simulations of large-scale LGIWs, the number of discrete numerical particles often exceeds several million (even 10 million) owing to the problem scale and complex terrain. Modeling in central processing unit (CPU) cores for massive particles and large-scale problems requires considerable computation time or even impossible. Therefore, it is essential to develop high performance computation for 3D SPH simulations of large-scale LGIW problems. In recent years, high performance GPUs have become increasingly widespread and utilized in SPH simulations (Mokos et al., 2015; S. Wang et al., 2021). The massive parallel and multi-thread architecture of GPUs has made it possible to simulate large-scale problems. As shown in Figure 1, a brief flowchart illustrates the process of running the GPU program. In this study, we implemented the soil–water coupling algorithm and landslide dynamics in the open-source GPU-accelerated SPH platform

Table 1
Algorithm of Computing Stress Rate

Step 1:

Obtain the grid size and block size depending on the number of particles, GSize and BSize.

GPU parallel is implemented through a CUDA kernel function, as follows.

kernel_name<<< GSize, BSize >>>(argument list).

Step 2:

Get a thread index within the CUDA kernel function.

p = blockIdx.y*gridDim.x*blockDim.x + blockIdx.x*blockDim.x + threadIdx.x.

Step 3:

Compute $\frac{d\sigma_p}{dt}$ through the corresponding physical variables at particle p.

DualSPHysics. The numerical algorithm of the main loop consists of the following steps: (a) generate the neighbor list; (b) calculate the interaction between water, soil, and boundary particles; (c) calculate the stress rate of soil particles; and (d) update the physical quantities of each particle. In comparison to the original DualSPHysics code, our program introduces several new interactions in step (b), including water–soil, soil–soil, soil–water, and soil–bound particle interactions. Additionally, we have also added the calculation of the strain rate tensor and spin rate tensor in step (b), as defined by Equations 10 and 11. Step (c) is newly implemented to compute the stress rate using Equation 8, while step (d) involves updating an additional stress variable for soil particles. The four steps were executed on a GPU device that mainly uses the CUDA (Computer Unified Device Architechture) kernel function to implement in parallel. As an example, Table 1 presents a concise framework for parallel computation of stress rate in step (c) above. We can control the threads in a CUDA kernel function by specifying the number of blocks and grids, as well as the number of threads in each block. By selecting the appropriate grid and block sizes, we were able to maximize the use of the GPU hardware and achieve high-performance computing in our simulation. In this work, a one-dimensional block size of 256 was chosen, and the two-dimensional grid size was determined based on the total number of particles. The thread index p corresponding to each particle index was then calculated using the grid and block size. Finally, the stress rate of particle p was computed in parallel for each thread. The more detailed program structure can be found in our previous contribution (Huang et al., 2022), in which the GPU-accelerated elastoplastic soil model was developed for large-scale landslides.

3. Validation Example

Granular material flow processes, such as landslides and avalanches, were simulated in our previous work (Huang et al., 2022) using an elastoplastic soil model. In this section, we report the validation of the interaction process of soil–water coupling using an experimental model.

Viroulet et al. (2013, 2014) reported the formation of a surge wave when a sliding body slid into a water tank, a process that has subsequently been simulated as a benchmark (Krimi et al., 2018). In the experiment, with the opening of a gate, the landslide body slowly slid into the water, generating surge waves and propagating along the flume. The initial sketch of this experiment is shown in Figure 2, where two wave gauges were arranged to observe the change in water surface elevation. The sliding mass in the experiment was composed of glass powder particles, and the relevant parameters are shown in Table 1. The glass beads with a diameter 4 mm have a high permeability coefficient in the order 10^{-1} m/s, which causes that mixing typically occurs very rapidly, within a short period of time. Therefore, the apparent mixed density of the slide was used in this simulation. The grain density ρ_g considers the bulk slide porosity $n = 0.4$; thus, the apparent density $\rho_s = \rho_g(1-n) + \rho_w n = 1,900$ kg/m^3 was used. The parameters c and φ were obtained from the experimental data of Viroulet et al. (2014), while typical soil parameters were applied for E and v. Herein, c was assigned a small value to achieve better numerical results. One case of $M_s = 2$ kg (M_s represents the mass of the sliding body, corresponding to $l_s = 0.165$ m) was
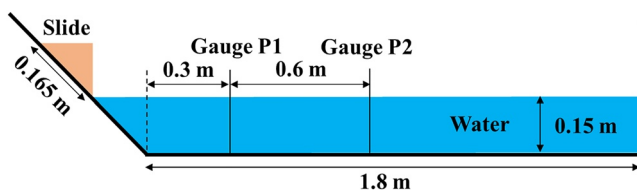

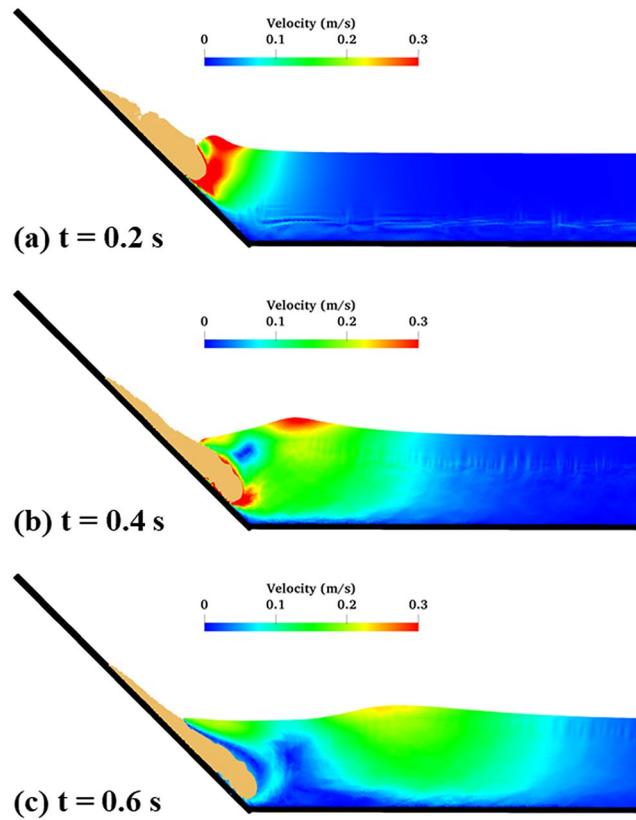**Figure 2.** Sketch of the experimental configuration (Viroulet et al., 2013).

Figure 3. Soil–water interaction and generation of the surge wave at three moments.

simulated herein. An initial particle distance dp = 0.002 m, and 85,698 SPH particles were established to model this process. The validation example was performed using a computing system with an Intel(R) Xeon(R) Gold 6226R CPU clocked at 2.90 GHz and an NVIDIA RTX A6000 GPU equipped with 48 GB of global memory and 84 multiprocessors running at a clock rate of 1.8 GHz. In this simulation, a block size of 256 and a grid size of (335, 1) were chosen to maximize GPU performance. The simulation was completed in 23.4 min.

Figure 3 shows three typical moments of the interaction process. This was a typical non-separation flow, that is, there was no cavity between the water and soil. The sliding mass started to squeeze the water body and formed a surge wave. The water climbed along the sliding mass and returned back forming a second wave. This physical process is consistent with experimental observations. Moreover, Figure 4 shows two plotted curves of water
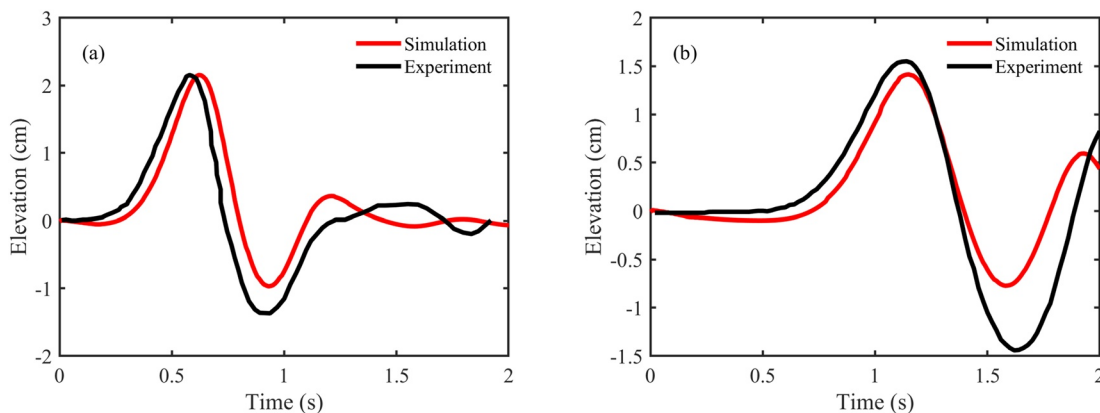

Figure 4. Wave height of gauge points with time. (a) Gauge P1; (b) Gauge P2.
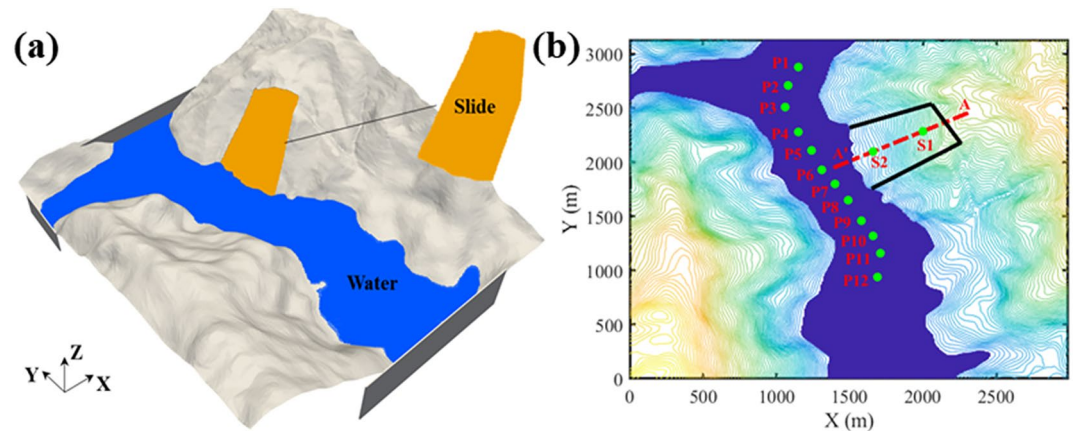
Figure 5. Initial configuration of the Huangtian landslide-generated impulse waves. (a) 3D view. (b) Contour map.

surface elevation with time at two wave gauges. The simulated results were in good agreement with the experimental curves, especially for the head-wave height, which is most critical in the study of surge disasters; this reflects the ability of the model to simulate the process of a low-speed landslide generating head waves. However, the wave obtained through simulated results for the two gauges had an obvious difference from the experimental results, especially for the second wave gauge. Because of an overestimation of the resistance of water to soil mass, the movement of the underwater slide mass is blocked, which leads to the formation of a smaller trough. In general, compared with the experimental results, the simulated curves of water surface elevation were satisfactory, especially that of head-wave elevation.

4. Simulation of Huangtian Landslide-Generated Surge Waves

4.1. Numerical Model Setup for Huangtian LGIWs

On 20 July 2009, affected by continuous rainfall, a mass of material at Huangtian on the right bank of the Lancang River, approximately 7.5 km upstream from the Xiaowan Hydropower Station, suddenly slipped. The impact triggered waves more than 30 m in height. The Huangtian landslide mass after sliding was approximately 500 m wide and 350 m high. Granular material within this landslide mainly consisted of rubble, with a diameter ranging from 2 cm to 2 m; the landslide had a total volume of more than 40 million m^3 (Y. Liu et al., 2015).

We used the local detailed topographic map before the landslide and large-scale topographic map provided by ASTER v2 for splicing. Our aim was to reproduce the entire generation process and near-field characteristics of the landslide-induced surge wave and provide additional information to that which could be obtained from a field survey (Y. Liu et al., 2015). Elevation data of the Huangtian terrain were established by selecting a computational domain of approximately 3×3 km with the Huangtian landslide as the center (Figure 5). Owing to the lack of a complete 3D slip surface, an initial cubic deposit volume was established (Figure 5a), while the terrain boundary and water body were obtained accurately. As shown in Figure 5b, an approximate linear profile of this landslide mass was obtained from Wu (2011). Twelve wave gauges (P1–P12) in the Lancang river and two gauges (S1 and S2) on the surface of the landslide mass were positioned to check the variation in elevation of the water and landslide. A typical cross-section A–A′ of the landslide was chosen (see Figure 5b) to study its behavior. The blue area in Figure 5a represents the water, with a hydrostatic water level of 1,160 m.

The soil parameters shown in Table 2 were obtained from Y. Liu et al. (2015), who measured mechanical parameters through experiments and field surveys. It is worth noting that the internal friction angle used in this paper is a little lower than the measured value, because the internal mechanisms of a large-scale landslide remain to be discovered (Lucas et al., 2014; X. Wang & Li, 2017; Zhang et al., 2018).

Table 2
Material Parameters Used in Our Numerical Simulations

Case	E (MPa)	φ (°)	c (kPa)	ψ (°)	v (-)	ρ (kg/m³)
Verification	20	23.3	0.02	0	0.3	1,900
Huangtian landslide	500	16	15	0	0.25	2,100

Table 3
Number of SPH Particles and the Corresponding Grid Size in Our Four Numerical Models

Particle distance (m)	Boundary	Soil	Water	Total	Grid size
7.5	1,307,002	298,446	508,418	2,113,866	(8,258,1)
5	2,871,322	1,006,495	1,688,863	5,566,680	(21,475,1)
4	4,502,278	1,976,560	3,286,714	9,765,552	(38,147,1)
3	7,925,266	4,710,213	7,958,777	20,594,256	(283,285)

4.2. Convergence Analysis

As mentioned previously, a number of 2D and 3D large-scale landslide problems have been simulated using the SPH method. In addition, LGIW processes have been simulated in some studies using a coupled fluid–solid model, where a rigid-body model was used for the landslide (Shi et al., 2015; Vacondio et al., 2013). In SPH simulations of large-scale geotechnical and geological engineering problems, the resolution of the coupled SPH model for LGIWs needs to be accurately considered to provide more reliable results. The numerical resolution of SPH simulations for large-scale landslides has recently been reported (Huang et al., 2022; Peng et al., 2021). To our knowledge, there have been no such reports for the soil–water coupled SPH model for large-scale LGIWs. Therefore, we here conducted convergence analysis and investigated the influence of numerical resolution.

Four numerical cases with different particle distances (dp = 7.5, 5, 4, and 3 m) were created, as listed in Table 3. The smoothing length for all simulations was taken as 1.5 times the initial particle distance. The whole physical time lasts 60 s, which was long enough to reflect soil–water interaction and the near-field characteristics of surge waves. All simulations were run on a workstation with NVIDIA RTX A6000 hardware (48 GB of global memory and 84 multiprocessors with a clock rate of 1.8 GHz). In the four simulations, a block size of 256 was chosen and the grid size was determined based on the total number of particles as listed in Table 3. Computation time for these four cases ranged from 0.4 to 23.2 hr. The final states of the four simulations are plotted in Figure 6, where the color of the water body represents water elevation, and the color of the landslide mass indicates accumulated plastic strain (Adps) (Huang et al., 2022), where $Adps = \int_0^t \sqrt{\frac{2}{3}\dot{\epsilon}^p : \dot{\epsilon}^p} dt$. From Figure 6, it can be seen that a small wave near to the opposite bank is captured from dp = 5 to 3 m, while the other water areas have a similar color map. Deformation characteristics are mainly concentrated on the two sides and upper surface of the landslide body. According to the color diagram of the sliding body, this feature can be fully observed at dp = 5 m. Furthermore, Figure 7 illustrates the differences in water surface and soil deposit elevations deviating from results of dp = 4 m as a base. A clear difference of the slice into the landslides as shown in Figures 7b and 7e reveal that the differences between results from dp = 5 m and dp = 4 m are minimal.

To investigate the influence of the landslide on the interaction between water and soil, final A–A′ cross-sections at different resolutions are shown in Figure 8. The internal deformation of the landslide mass can be described by Adps. It can be seen that the color of the middle shear band deepens significantly as the initial particle distance becomes smaller, which may be attributed to the accumulation of numerical errors (Feng et al., 2022). Peng et al. (2021) have also pointed out that the particle size-dependency in SPH modeling of large-scale landslides has a strong impact on the shear strain since the particle size determines the thickness of the basal shear zone. Nevertheless, the positions of the sliding zone are mostly consistent, to some extent, indicating the reliability of the simulation results. Figures 9a and 9b depict the final soil deposit and water surface profiles at different resolutions, which indicates the good consistency. Figures 9c and 9d further display the corresponding differences, revealing that resolutions of dp = 5, 4, and 3 m are nearly identical.

Furthermore, Figure 10 shows the elevation curves of the two measuring points (S1 and S2 in Figure 5) with time in this cross-section for different simulations; good convergence is also found for these data. At point S1, there is a rapid elevation increase because of the initiation of the landslide mass at higher elevation. At the low elevation point (S2), the elevation shows a rapid decrease, which implies that the material from this lower slope slides directly into the water body.

For the water body, we mainly investigated the relationship between wave height and time at different measuring points. The variation in wave height at four gauging points is plotted in Figure 11. These four typical points were evenly distributed in the production and propagation zones. For the case dp = 7.5 m, the curves, especially
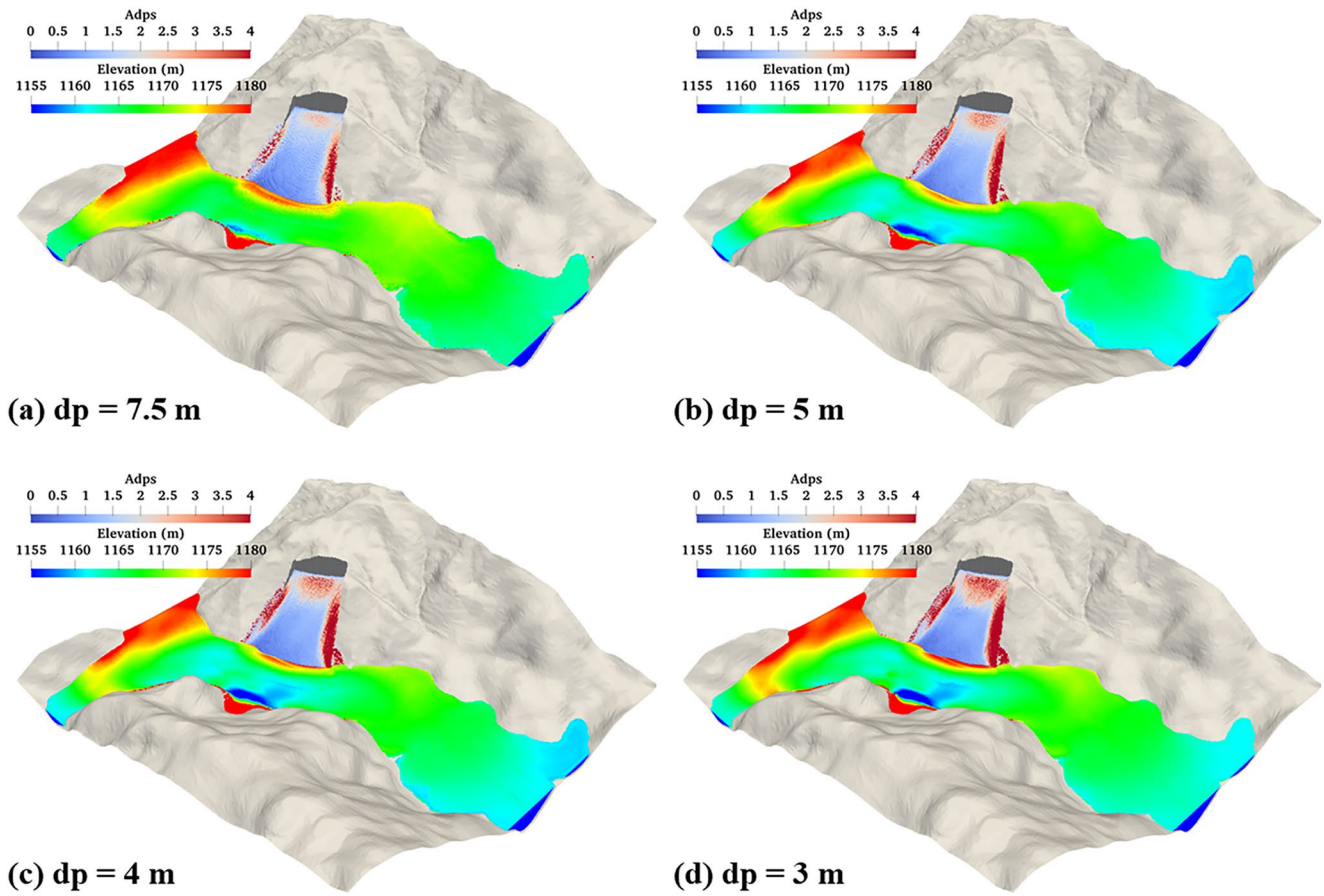
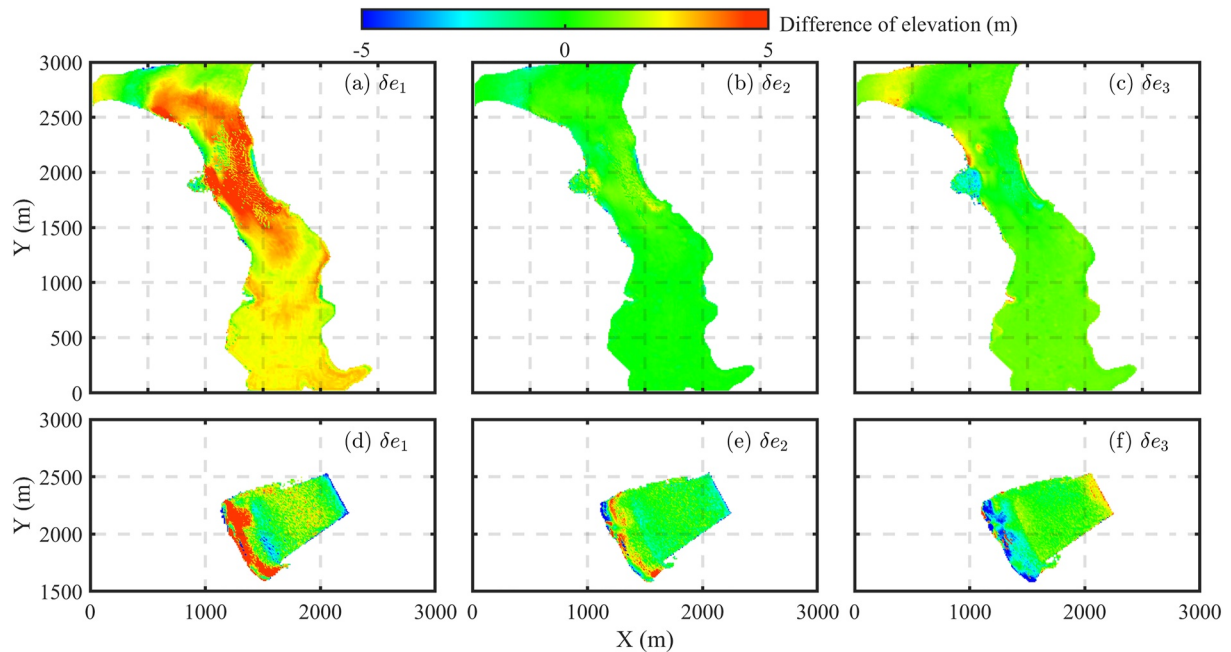**Figure 6.** Final states from simulations with different numerical resolutions.

Figure 7. Difference maps of water surface and soil deposit elevations, where δe_1, δe_2, and δe_3 represent the differences between a resolution of 7.5, 5, and 3 m, respectively, and a resolution of 4 m. Panels (a)–(c) represent the water surface elevation, while (d)–(f) represent the differences in soil deposit elevation.
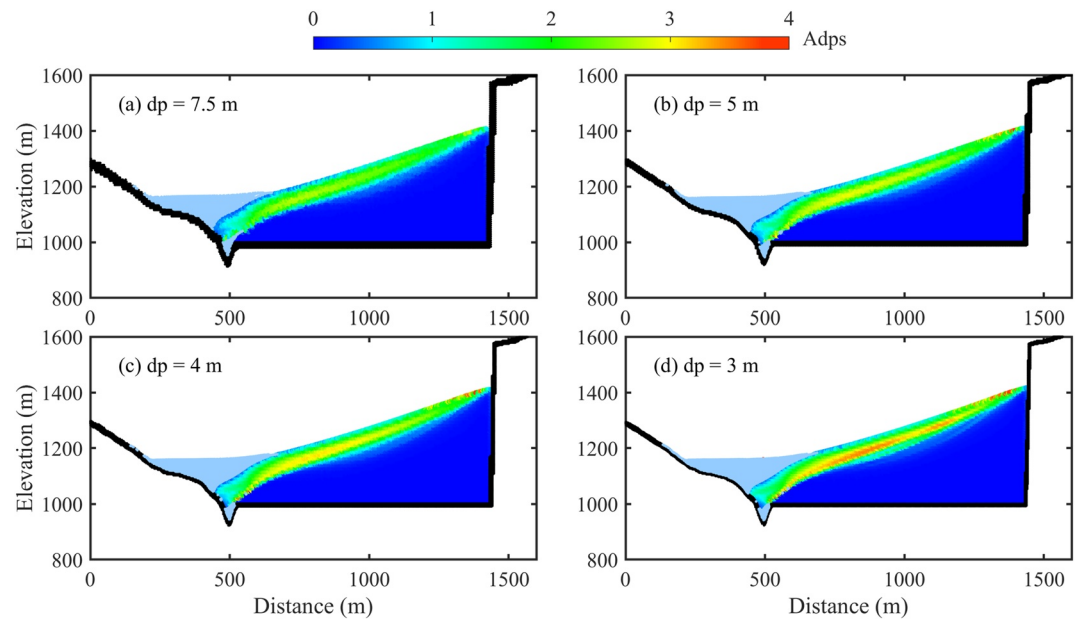
Figure 8. Final deposit of the landslide at the A–A′ cross-section for different simulations.
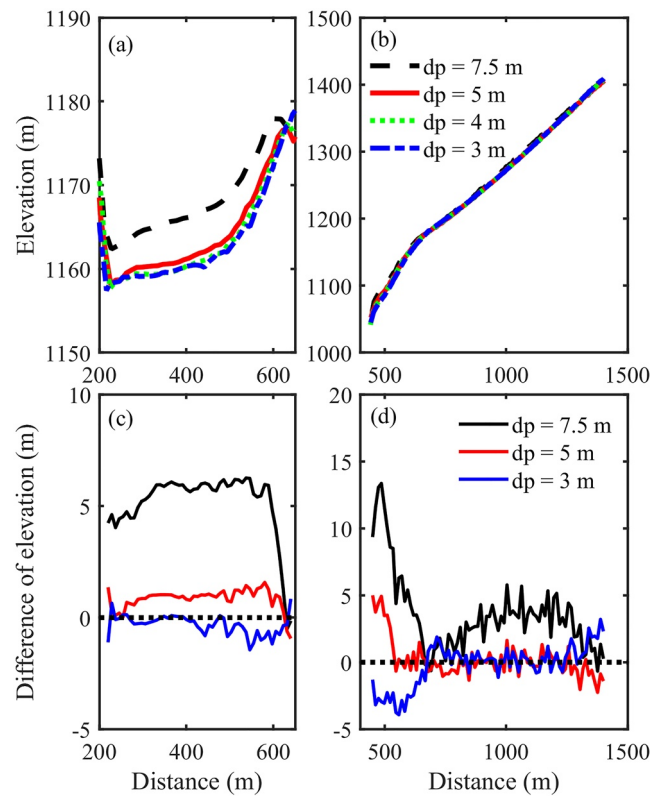

Figure 9. Soil deposit and water surface profiles and corresponding differences at different resolutions. Panels (a) and (b) represent the final profiles of water surface and soil deposit; panels (c) and (d) represent the differences of water surface and soil deposit in elevation, where δe_1, δe_2, and δe_3 represent the differences between a resolution of 7.5, 5, and 3 m, respectively, and a resolution of 4 m.
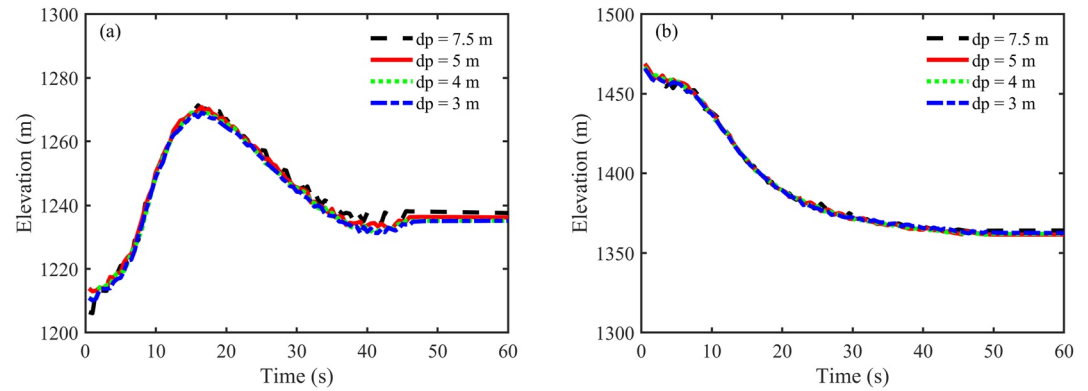
Figure 10. Elevation of soil surface with time for different numerical resolutions. (a) S1. (b) S2.

at P5 and P8, show an obvious difference compared with the other three simulations. From dp = 5 to 3 m, the wave height peaks retain almost the same value; it was also found that the wave trough depended on the initial particle distance. However, the focus is generally placed on maximum wave height owing to the large energies involved when studying LGIW problems. The convergence about wave height implies that a particle distance of 5 m is sufficient for simulating the Huangtian LGIW.

From this convergence analysis, we found that it was important to determine an appropriate particle distance for this soil-coupling problem in SPH simulations, which can reduce the calculation time while still ensuring accuracy. The results of the convergence analysis show that in the Huangtian LGIW, a particle distance dp = 5 m is sufficient. In other large-scale landslide simulations using the SPH method with elastoplastic closure, particle distances of 3.3 and 8 m have been reported for the Baige landslide (Peng et al., 2021) and Yigong avalanche (Huang et al., 2022), respectively, corresponding to an approximate slide volume of 27.6 and 300 million m^3. Our convergence analysis for the Huangtian LGIW is, to the best of our knowledge, a first for the study of complex
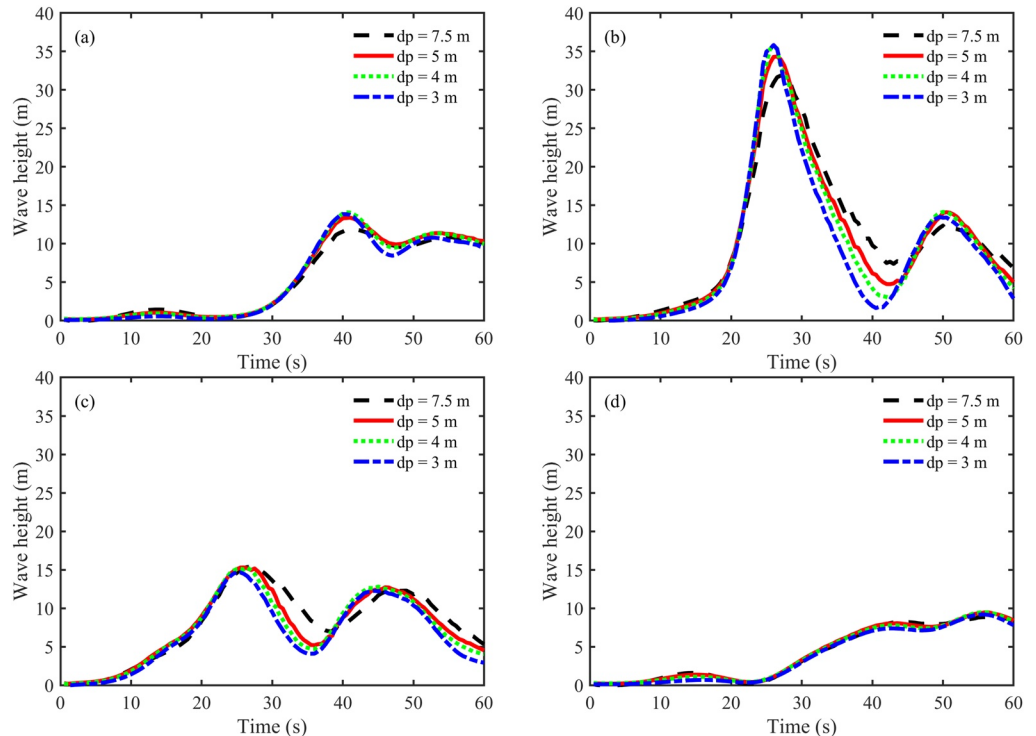

Figure 11. Relationship of wave height with time for different points in the river. (a) P2. (b) P5. (c) P8. (d) P11.
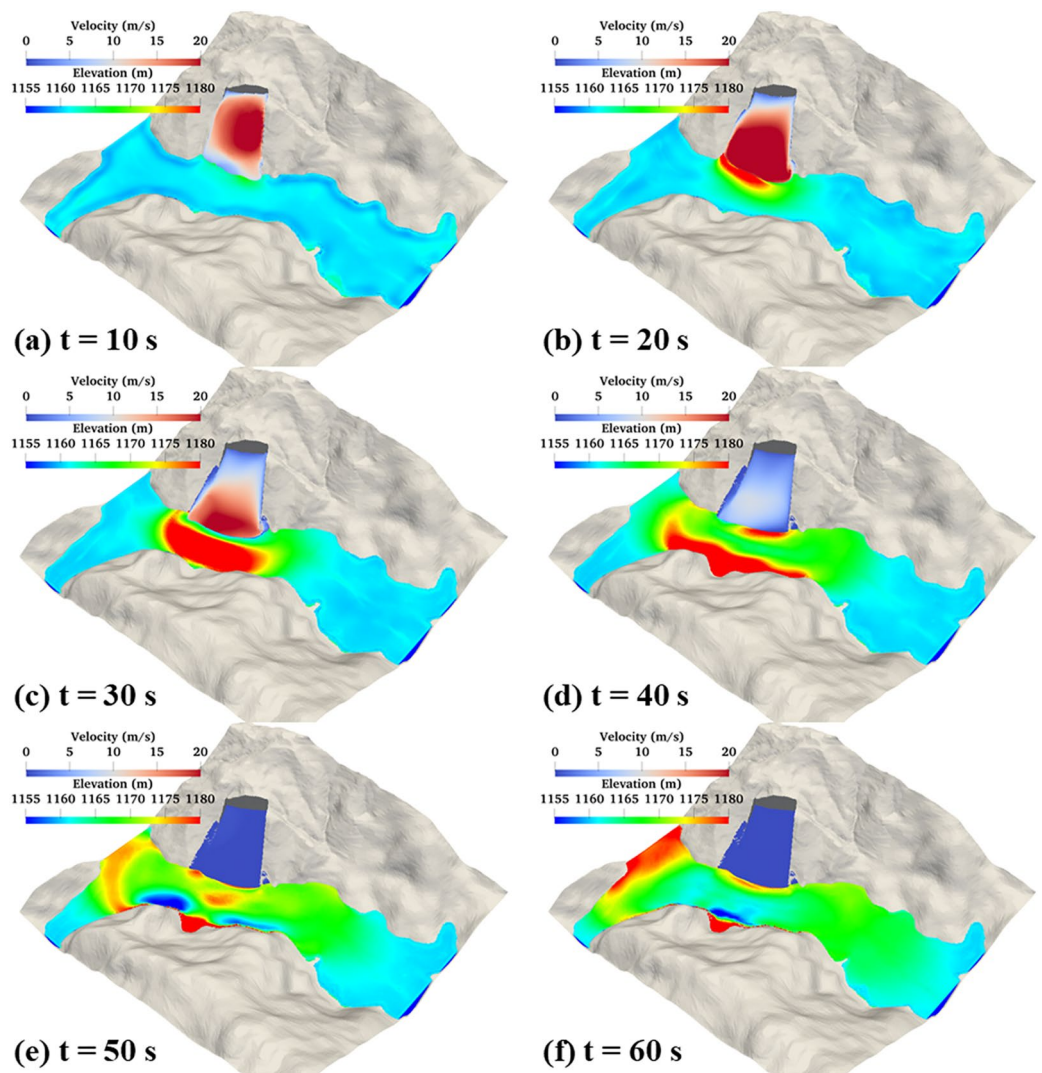
Figure 12. Flow process of the Huangtian landslide-generated impulse waves at six typical moments.

soil–water coupling problems using the SPH method. This may provide a reference for selecting an initial particle distance in SPH simulations of other LGIWs of similar scale 41.6 million m^3. Therefore, the scale of the landslide may be a primary factor in choosing an appropriate particle distance. According to our understanding, in SPH simulations of large-scale geotechnical engineering problems, convergence analysis depends on many factors and is typically performed on a case-by-case basis. Although there are several references available for simulating large-scale landslides, it is still recommended to perform a convergence analysis when dealing with different large-scale LGIW problems. The GPU-accelerated technology utilized herein provides the possibility to perform convergence analysis of large-scale simulations or use smaller particle distances.

4.3. Generation and Propagation of the Surge Wave

As mentioned above, an initial particle distance dp = 5 m was selected to simulate the Huangtian LGIW. In this section, the entire process, including landslide, soil–water interaction, generation of wave, and wave propagation, will be described in detail. Figure 12 shows the temporal evolution of water wave elevation in the reservoir and variation in sliding velocity at different sliding stages, corresponding to 10, 20, 30, 40, 50, and 60 s, respectively. Figure 13 shows the distributions of water velocity and Adps of the landslide mass in the A–A′ cross-section at six typical moments.
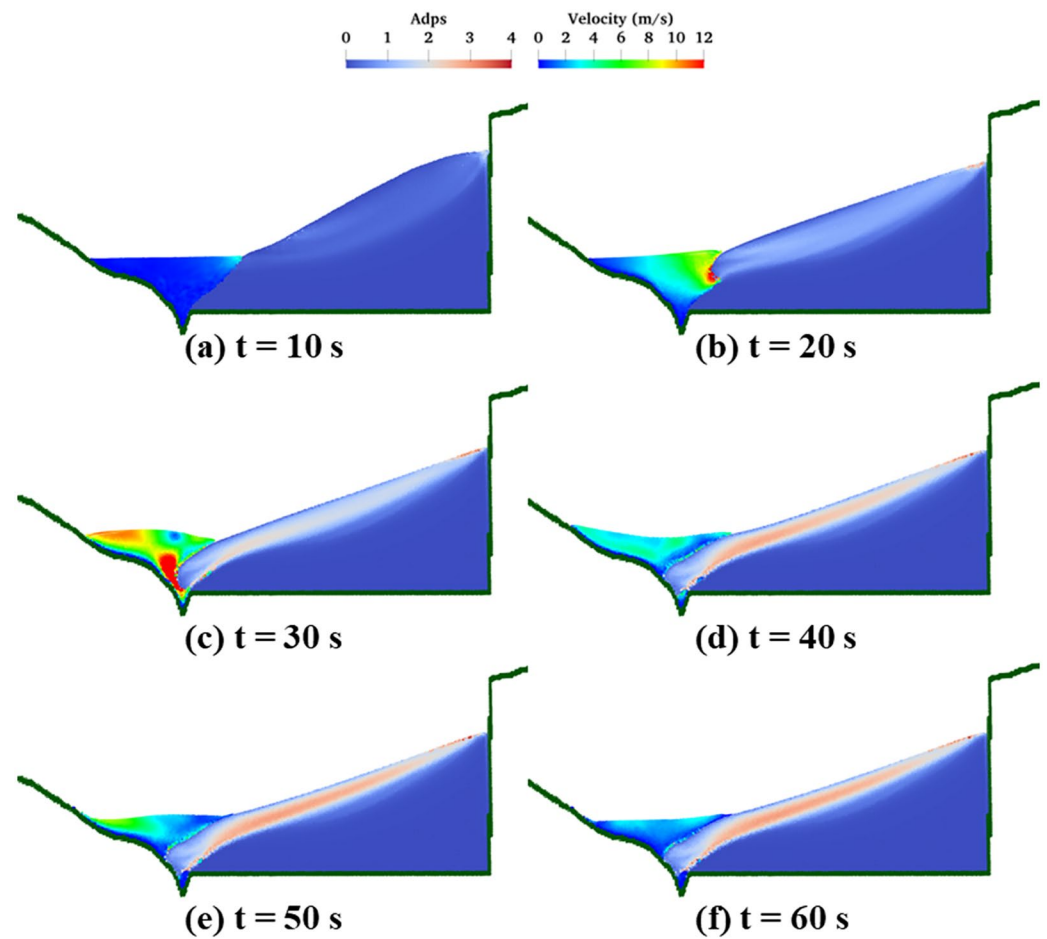
Figure 13. Evolution process of the A–A′ cross-section at six different moments.

From these two figures, it can be seen that the landslide mass began to destabilize under the action of gravity within the first 10 s, and granular material on the surface obtained an initial velocity of approximately 15–20 m/s, while the water body showed almost no variation during this time. Figure 13a shows an inconspicuous slip line that confirms the instability of the sliding mass. At $t = 20$ s, an obvious slip line can be observed in Figure 13b; part of the sliding mass entered the water, and a circular water wave propagated owing to high-speed compression of the front edge of the sliding body. From 20 to 30 s, the sliding mass continued to enter the water, squeezing the water body and producing a surge wave that spread forward. The generated wave mainly propagated to the opposite bank, and only a small part propagated upstream and downstream. The water body near to the sliding mass achieved a high velocity of approximately 10 m/s owing to compression, and a bump on the water surface can be observed in Figure 13c. At approximately 40 s, the head wave reached the opposite bank and climbed to its highest point. Meanwhile, the landslide had almost stopped moving; only a small proportion of the material on the surface was still moving at low speed (Figure 13d). After $t = 40$ s, backflow occurred in the interaction zone, causing a second wave in this area (Figures 12e and 13e), and the head wave propagated upstream and downstream.

Figure 14 shows the wave height variation curves of 12 measuring points, whose detailed location coordinates can be found in Figure 5b. According to location, we divided the 12 points into three groups: upstream propagation area, generation area, and downstream propagation area. In the upstream zone (P1–P4), P4 recorded the maximum wave height because it is adjacent to the production area. As the distance upstream increased, the wave height decayed exponentially. In the interaction zone, two significant wave peaks can be observed in Figure 14b. As mentioned above, the head wave propagated to the opposite bank, climbed, and returned, causing the second smaller wave. It is worth noting that the maximum wave height decreased in the generation area moving from P5
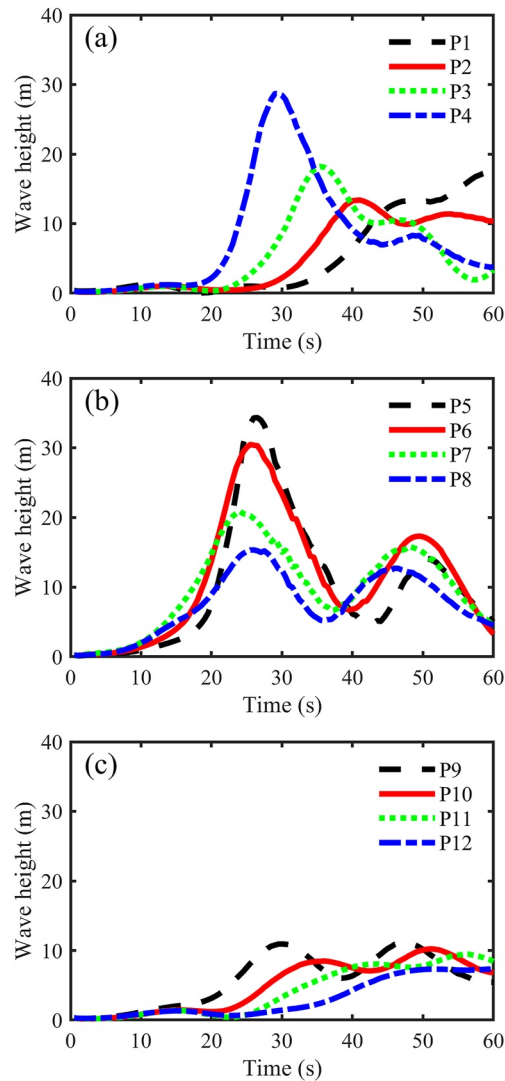
Figure 14. Wave height at the 12 measuring points with time. (a) P1–P4. (b) P5–P8. (c) P9–P12.

to P8, which implies that more soil slid into the water in the upstream area. This can be confirmed from Figure 12, which indicates that the velocity distribution of the sliding body was mainly concentrated in the upper part and the water waves propagated mainly upstream. The peak value of the head wave also decreased in the same manner as for points P1–P4.

From the perspective of energy distribution, the maximum wave height at P4, P5, and P6 exceeded 20 m, indicating that most of the energy for the water body was generated by the landslide in the interaction zone. In the propagation zone, the maximum wave height was lower than 20 m, and only approximately 10 m in the downstream zone. Therefore, the energy of the Huangtian LGIW was concentrated in the interaction zone, and only a small part of the energy propagated upstream and downstream as water waves. In other words, the opposite bank is more vulnerable to damage than the upstream and downstream areas.

From the above analysis, this simulation comprehensively shows that the sliding body loses stability, slides, enters the water, generates a surge wave, and the surge wave propagates. The velocity of the sliding mass in the flow process was as high as 20 m/s. The maximum wave height occurred in the generation area and gradually decreased both upstream and downstream. The run-up height of the wave on the opposite bank reached approximately 48 m. However, at the farthest measuring points of P1 and P12, there was a wave height of only approximately 7–10 m. For this narrow river, the landslide-generated surge wave mainly affected the opposite bank, and only a relatively small wave propagated along the river.
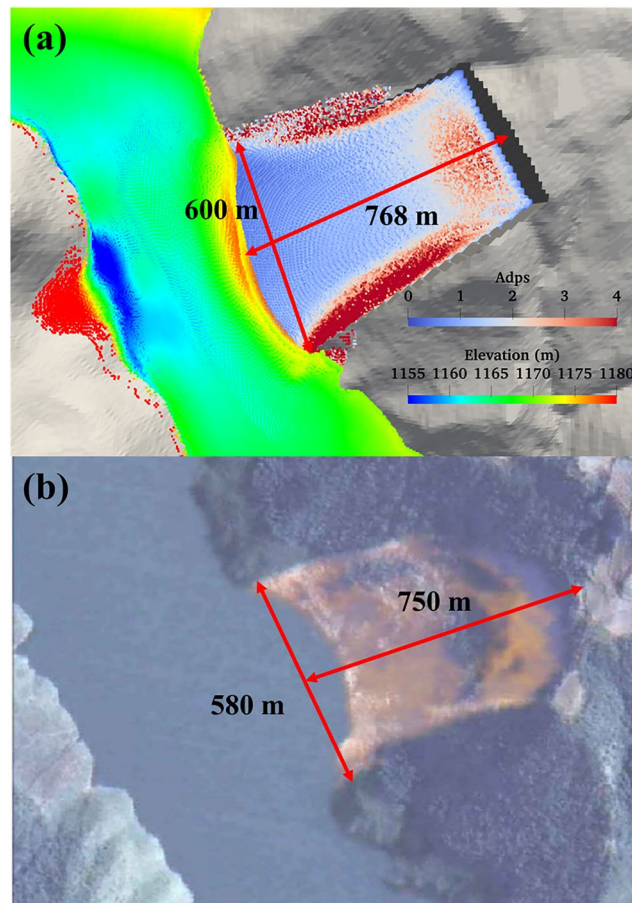
Figure 15. Final deposit of the Huangtian landslide. (a) Simulated results. (b) Field data (Wu, 2011).

4.4. Comparisons With Field Survey and Rigid LGIW Model Results

A real-world LGIW process always occurs accidently, unpredictable in geographical location, and often lacks observational data. Only a very limited amount of data were reported for the typical Huangtian LGIW, both for the landslide and resultant water wave (Y. Liu et al., 2015; Wu, 2011). Convergence analysis, the generation and development of surge waves have been discussed in the previous two sections. This section provides a comparison of the finite observations with the simulation results for both the landslide and surge wave.
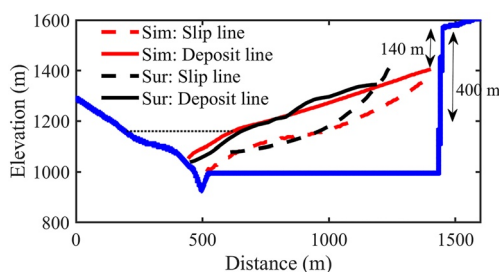
The top view of the final deposit of the simulated Huangtian landslide is shown in Figure 15, together with the observed deposit. Although very roughly, there was still good agreement between the field observation and simulation, where the width and length of the landslide mass were approximately 600 and 768 m, respectively. The deposit height of landslide mass above the hydrostatic reservoir surface was approximately 400 m (Figure 16). Figure 16 shows a comparison between the simulation results and field survey for the deposit and slip lines within a 2D cross section. The simulated slip line was chosen as the dividing line, with Adps = 0.2 representing the shearing zone. The simulated results compare well with the field survey. The rear of the landslide shows a large difference because the 2D cross sections do not precisely match between the simulation and field survey. The simulated results show that the height of the steep wall at the rear edge of the landslide was approximately 140 m, a slight overestimation compared with the survey data (115 m).
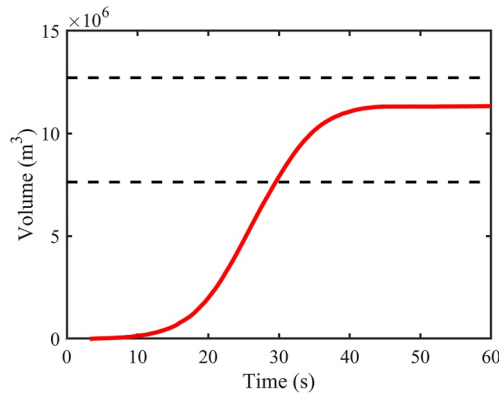

Figure 16. Final profile and slip line of the simulation compared with the field survey. Blue points represent simulated boundary.

Figure 17. Volume of landslide mass entering the water with time.

We also estimated the total slip volume and inflow volume through the A–A′ cross-section diagram provided by Y. Liu et al. (2015). As mentioned above, the final total sliding volume was calculated by counting the portion with Adps greater than 0.2, and the volume of landslide mass entering the water was computed as the volume of soil minus the initial volume below the still water level (1,160 m). The total slide volume was approximately 41.6 million m^3, which is within the estimated range of 38.1–63.6 million m^3 obtained from the field survey (Y. Liu et al., 2015). A wide range for the field results is plotted in Figure 17, where the dashed lines represent the upper and lower estimated values. This shows that the final simulated volume of landslide mass entering into the water was 11.3 million m^3, which is within the estimated range of 7.6–12.7 million m^3 (Y. Liu et al., 2015). Moreover, the water entry process took place from 10 to 40 s, which corresponds to the surge wave analysis presented above.

We further compared the characteristics, maximum wave height, and run-up height of the surge waves. Figure 18 shows the maximum wave height at different measuring points, where two dashed black lines represent the estimated range of maximum wave height according to the field survey (Wu, 2011). Because the field survey did not provide the position of the observed surge wave, we used the maximum wave heights at all 12 measuring positions in the near field of the LGIW for comparison. The maximum wave height of the surge wave was approximately 34.3 m at P5, located between the two dashed black lines (Figure 18). The maximum wave height of the simulated surge wave at P4 and P6 was approximately 30 m, which is also close to the field survey result. For other measuring points, the maximum wave heights were somewhat lower than the field estimates. Therefore, we infer that the observation position for the maximum wave height in the field survey was close to P5. Wave run-up height at the opposite bank of the A–A′ cross-section is plotted in Figure 19, which shows that the maximum simulated run-up height was approximately 48 m, slightly larger than the range estimated from the field survey (38.4–44.3 m; Y. Liu et al., 2015).

Through analyzing the characteristics of the simulated landslide mass and maximum wave height, we see a good consistency with field data. Here, we discuss the differences between the surge characteristics simulated by the fluid–rigid-body coupling model and soil–water coupling model. Shi et al. (2015) simulated the Huangtian LGIW using a fluid–rigid-body SPH coupling model. Such fluid–rigid-body coupling models usually require assumptions of landslide volume, slip surface, and sliding velocity in advance. It is difficult to obtain these preconditions from field surveys, while estimated results obtained using various empirical methods may vary substantially (Wu, 2011). One significant advantage of the deformed-body model is that it does not require many initial assumptions for landslide dynamics. The present model can simulate the landslide dynamics, including large deformation, flow, and interaction with water motion, which improves the rigid-body model for landslides.

For surge wave characteristics, one obvious difference is that this study shows a secondary wave in the interaction zone that was not observed in the work of Shi et al. (2015). As mentioned in Section 4.3, secondary waves are caused by backflow. The rigid-body model underestimates both the entry velocity and the volume sliding into the water body, which leads to a smaller run-up height on the opposite bank and little backflow. The maximum run-up height in Shi et al. (2015) was approximately 21.4 m, while this study determined it to be 48 m, which is closer to the field observation (Y. Liu et al., 2015). In terms of the opposite bank run-up height and secondary wave simulation, the soil–water coupling model performs better than the rigid-body model.

Numerical results obtained using the rigid-body model showed that the surge wave propagated with almost the same value upstream and downstream (Shi et al., 2015). Owing to the uneven terrain distribution and deformation of the sliding mass, surge waves do not propagate symmetrically upstream and downstream. The simulation results obtained using the present model are more reasonable, that is, the wave heights upstream and downstream are different.

To briefly summarize, the model presented herein can better describe the whole process of LGIW from landslide dynamics, interface interaction, surge generation and propagation than the rigid-body model. Therefore, it is advantageous to use the deformed-body model to simulate such LGIW problems.
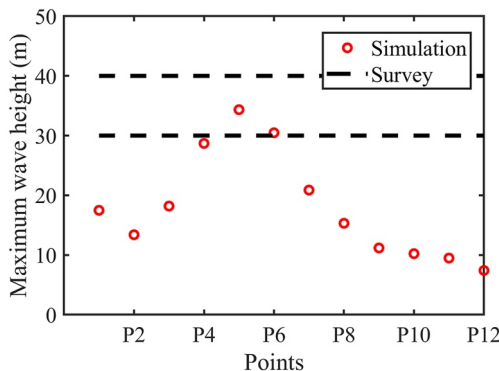

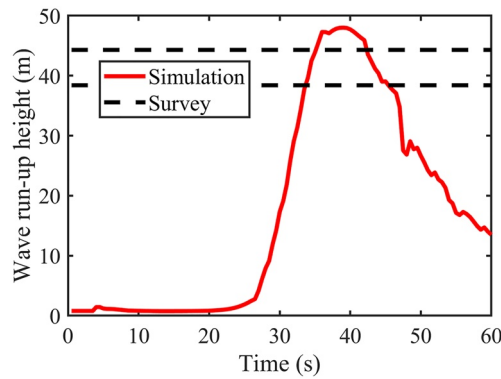**Figure 18.** Maximum wave height at different measuring points.

Figure 19. Wave run-up height at the opposite bank of cross-section A–A'.

5. Conclusions

To simulate a large-scale LGIW, we improved our former soil–water coupling SPH model via a novel treatment of soil–water interface interaction, which is implemented by the GPU-accelerated technique on the DualSPHysics (v4.0) platform. This new coupled accelerated SPH model provides enhanced capability for large-scale LGIW problem simulation; the spatial scale can be increased to hundreds of meters or even kilometers for landslides, soil–water interface coupling, and water wave generation, with more than 20 million SPH particles and a computing time of lower than 24 hr. Using this newly developed coupled accelerated SPH model, a real-world large-scale LGIW case (Huangtian LGIW) was simulated to quantitatively reproduce the entire disaster chain process, including landslide dynamics, fluid–solid interaction, and surge wave generation. Convergence analysis of the Huangtian LGIW demonstrated that a particle distance of 5 m was sufficiently fine to provide a reliable deposition distribution and variation in wave height; this can provide a reference for particle distance setup for other similar large-scale LGIW simulations. From simulation of the Huangtian LGIW, the landslide deposit was approximately 41.6 million m^3 in volume, 600 m in width, 768 m in length, and 400 m above the still water line, with an immersed volume of 11.3 million m^3; the maximum surge wave and run-up heights were 34.3 and 48 m, respectively. The computed results of the Huangtian LGIW were within the estimated ranges for both the landslide and surge wave obtained from a field survey. The proposed model provides a method for the whole LGIW disaster prediction from landslide initiation to wave generation in engineering geology scale, which is helpful for LGIW hazard assessment.

It should be noted that the current state-of-the-art in convergence analysis for simulating LGIW and landslide dynamics at the engineering geological scale using the SPH method still relies on a case-by-case approach, which differs significantly from the mesh dependence analysis in mesh-based methods. The case study of the large-scale Huangtian LGIW provides a reference on how to produce reliable information on landslide dynamics, interface coupling behavior, and surge wave characteristics using SPH method.

Data Availability Statement

The open-source code DualSPHysics version 4.0 (Crespo et al., 2015) was used in this manuscript, available at https://dual.sphysics.org/downloads/. The experimental data of verification example are available from Viroulet et al. (2014). Field survey data of Huangtian LGIW are available from Y. Liu et al. (2015). Local topographic data of Huangtian can be available through Figshare at Huang (2023), which are extracted using Global Mapper v10.02 from the public ASTER GDEMv2 30M resolution digital elevation data repository hosted by Geospatial Data Cloud, Computer Network Information Center, Chinese Academy of Sciences (http://www.gscloud.cn/).

References

Adami, S., Hu, X. Y., & Adams, N. A. (2012). A generalized wall boundary condition for smoothed particle hydrodynamics. *Journal of Computational Physics*, *231*(21), 7057–7075. https://doi.org/10.1016/j.jcp.2012.05.005

An, Y., Wu, Q., Shi, C., & Liu, Q. (2016). Three-dimensional smoothed-particle hydrodynamics simulation of deformation characteristics in slope failure. *Géotechnique*, *66*(8), 670–680. https://doi.org/10.1680/jgeot.15.P.222

Ataie-Ashtiani, B., & Najafi-Jilani, A. (2008). Laboratory investigations on impulsive waves caused by underwater landslide. *Coastal Engineering*, *55*(12), 989–1004. https://doi.org/10.1016/j.coastaleng.2008.03.003

Bu, S., Li, D., Chen, S., Xiao, C., & Li, Y. (2022). Numerical simulation of landslide-generated waves using a SPH-DEM coupling model. *Ocean Engineering*, *258*, 111826. https://doi.org/10.1016/j.oceaneng.2022.111826

Bui, H. H., Fukagawa, R., Sako, K., & Ohno, S. (2008). Lagrangian meshfree particles method (SPH) for large deformation and failure flows of geomaterial using elastic-plastic soil constitutive model. *International Journal for Numerical and Analytical Methods in Geomechanics*, *32*(12), 1537–1570. https://doi.org/10.1002/nag.688

Bui, H. H., Fukagawa, R., Sako, K., & Wells, J. C. (2011). Slope stability analysis and discontinuous slope failure simulation by elasto-plastic smoothed particle hydrodynamics (SPH). *Géotechnique*, *61*(7), 565–574. https://doi.org/10.1680/geot.9.P.046

Chen, J.-Y., Lien, F.-S., Peng, C., & Yee, E. (2020). GPU-accelerated smoothed particle hydrodynamics modeling of granular flow. *Powder Technology*, *359*, 94–106. https://doi.org/10.1016/j.powtec.2019.10.017

Chen, W., & Qiu, T. (2012). Numerical simulations for large deformation of granular materials using smoothed particle hydrodynamics method. *International Journal of Geomechanics*, *12*(2), 127–135. https://doi.org/10.1061/(asce)gm.1943-5622.0000149

Crespo, A. J. C., Domínguez, J. M., Rogers, B. D., Gómez-Gesteira, M., Longshaw, S., Canelas, R., et al. (2015). DualSPHysics: Open-source parallel CFD solver based on smoothed particle hydrodynamics (SPH). *Computer Physics Communications*, *187*, 204–216. https://doi.org/10.1016/j.cpc.2014.10.004

Feng, R., Fourtakas, G., Rogers, B. D., & Lombardi, D. (2022). Two-phase fully-coupled smoothed particle hydrodynamics (SPH) model for unsaturated soils and its application to rainfall-induced slope collapse. *Computers and Geotechnics*, *151*, 104964. https://doi.org/10.1016/j.compgeo.2022.104964

Fritz, H. M., Hager, W. H., & Minor, H.-E. (2001). Lituya Bay case: Rockslide impact and wave run-up. *Science of Tsunami Hazards*, *19*(1), 3–22.

Fritz, H. M., Hager, W. H., & Minor, H. E. (2004). Near field characteristics of landslide generated impulse waves. *Journal of Waterway, Port, Coastal, and Ocean Engineering*, *130*(6), 287–302. https://doi.org/10.1061/(asce)0733-950x(2004)130:6(287)

Han, L., & Hu, X. (2018). SPH modeling of fluid-structure interaction. *Journal of Hydrodynamics*, *30*(1), 62–69. https://doi.org/10.1007/s42241-018-0006-9

Heller, V., Bruggemann, M., Spinneken, J., & Rogers, B. D. (2016). Composite modelling of subaerial landslide–tsunamis in different water body geometries and novel insight into slide and wave kinematics. *Coastal Engineering*, *109*, 20–41. https://doi.org/10.1016/j.coastaleng.2015.12.004

Heller, V., & Spinneken, J. (2013). Improved landslide-tsunami prediction: Effects of block model parameters and slide model. *Journal of Geophysical Research: Oceans*, *118*(3), 1489–1507. https://doi.org/10.1002/jgrc.20099

Heller, V., & Spinneken, J. (2015). On the effect of the water body geometry on landslide–tsunamis: Physical insight from laboratory tests and 2D to 3D wave parameter transformation. *Coastal Engineering*, *104*, 113–134. https://doi.org/10.1016/j.coastaleng.2015.06.006

Huang, C. (2023). Numerical simulation of the large-scale Huangtian (China) landslide-generated impulse waves by a GPU-accelerated three-dimensional soil–water coupled SPH model [Dataset]. Figshare. https://doi.org/10.6084/m9.figshare.21571344.v5

Huang, C., & Liu, M. B. (2020). Modeling hydrate-bearing sediment with a mixed smoothed particle hydrodynamics. *Computational Mechanics*, *66*(4), 877–891. https://doi.org/10.1007/s00466-020-01895-1

Huang, C., Sun, Y., An, Y., Shi, C., Feng, C., Liu, Q., et al. (2022). Three-dimensional simulations of large-scale long run-out landslides with a GPU-accelerated elasto-plastic SPH model. *Engineering Analysis with Boundary Elements*, *145*, 132–148. https://doi.org/10.1016/j.enganabound.2022.09.018

Krimi, A., Khelladi, S., Nogueira, X., Deligant, M., Ata, R., & Rezoug, M. (2018). Multiphase smoothed particle hydrodynamics approach for modeling soil–water interactions. *Advances in Water Resources*, *121*, 189–205. https://doi.org/10.1016/j.advwatres.2018.08.004

Liu, M., Shao, J., & Chang, J. (2012). On the treatment of solid boundary in smoothed particle hydrodynamics. *Science China Technological Sciences*, *55*(1), 244–254. https://doi.org/10.1007/s11431-011-4663-y

Liu, Y., Wu, J., & Li, H. (2015). Surge prediction study of reservoir bank landslide near a hydropower dam. *Advances in Geosciences*, *05*(03), 114–129. (In Chinese). https://doi.org/10.12677/ag.2015.53015

Lucas, A., Mangeney, A., & Ampuero, J. P. (2014). Frictional velocity-weakening in landslides on Earth and on other planetary bodies. *Nature Communications*, *5*(1), 3417. https://doi.org/10.1038/ncomms4417

Mahallem, A., Roudane, M., Krimi, A., & Gouri, S. A. (2022). Smoothed particle hydrodynamics for modelling landslide–water interaction problems. *Landslides*, *19*(5), 1249–1263. https://doi.org/10.1007/s10346-021-01807-1

McFall, B. C., & Fritz, H. M. (2017). Runup of granular landslide-generated tsunamis on planar coasts and conical islands. *Journal of Geophysical Research: Oceans*, *122*(8), 6901–6922. https://doi.org/10.1002/2017jc012832

McFall, B. C., Mohammed, F., Fritz, H. M., & Liu, Y. (2018). Laboratory experiments on three-dimensional deformable granular landslides on planar and conical slopes. *Landslides*, *15*(9), 1713–1730. https://doi.org/10.1007/s10346-018-0984-2

Minatti, L., & Paris, E. (2015). A SPH model for the simulation of free surface granular flows in a dense regime. *Applied Mathematical Modelling*, *39*(1), 363–382. https://doi.org/10.1016/j.apm.2014.05.034

Mohammed, F., & Fritz, H. M. (2012). Physical modeling of tsunamis generated by three-dimensional deformable granular landslides. *Journal of Geophysical Research*, *117*(C11), n/a. https://doi.org/10.1029/2011jc007850

Mokos, A., Rogers, B. D., Stansby, P. K., & Domínguez, J. M. (2015). Multi-phase SPH modelling of violent hydrodynamics on GPUs. *Computer Physics Communications*, *196*, 304–316. https://doi.org/10.1016/j.cpc.2015.06.020

Monaghan, J. J. (2005). Smoothed particle hydrodynamics. *Reports on Progress in Physics*, *68*(8), 1703–1759. https://doi.org/10.1088/0034-4885/68/8/r01

Monaghan, J. J., & Kos, A. (1999). Solitary waves on a Cretan Beach. *Journal of Waterway, Port, Coastal and Ocean Engineering*, *125*(3), 145–155. https://doi.org/10.1061/(ASCE)0733-950X(1999)125:3(145)

Nonoyama, H., Moriguchi, S., Sawada, K., & Yashima, A. (2015). Slope stability analysis using smoothed particle hydrodynamics (SPH) method. *Soils and Foundations*, *55*(2), 458–470. https://doi.org/10.1016/j.sandf.2015.02.019

Panizzo, A., Girolamo, P. D., Risio, M. D., Maistri, A., & Petaccia, A. (2005). Great landslide events in Italian artificial reservoirs. *Natural Hazards and Earth System Sciences*, *5*(5), 733–740. https://doi.org/10.5194/nhess-5-733-2005

Peng, C., Guo, X., Wu, W., & Wang, Y. (2016). Unified modelling of granular media with smoothed particle hydrodynamics. *Acta Geotechnica*, *11*(6), 1231–1247. https://doi.org/10.1007/s11440-016-0496-y

Peng, C., Li, S., Wu, W., An, H., Chen, X., Ouyang, C., & Tang, H. (2021). On three-dimensional SPH modelling of large-scale landslides. *Canadian Geotechnical Journal*, *59*(1), 24–39. https://doi.org/10.1139/cgj-2020-0774

Peng, C., Wu, W., Yu, H.-S., & Wang, C. (2015). A SPH approach for large deformation analysis with hypoplastic constitutive model. *Acta Geotechnica*, *10*(6), 703–717. https://doi.org/10.1007/s11440-015-0399-3

Risio, M. D., & Sammarco, P. (2008). Analytical modeling of landslide-generated waves. *Journal of Waterway, Port, Coastal, and Ocean Engineering*, *134*(1), 53–60. https://doi.org/10.1061/(ASCE)0733-950X(2008)134:1(53)

Shao, S. (2012). Incompressible smoothed particle hydrodynamics simulation of multifluid flows. *International Journal for Numerical Methods in Fluids*, *69*(11), 1715–1735. https://doi.org/10.1002/fld.2660

Shi, C., An, Y., Wu, Q., Liu, Q., & Cao, Z. (2016). Numerical simulation of landslide-generated waves using a soil–water coupling smoothed particle hydrodynamics model. *Advances in Water Resources*, *92*, 130–141. https://doi.org/10.1016/j.advwatres.2016.04.002

Shi, C., An, Y., & Yang, J. (2015). A SPH based numerical method of landslide induced impulse wave and its application on Huangtian landslide event. *SCIENTIA SINICA Physica, Mechanica & Astronomica*, *45*(10), 104706. (In Chinese). https://doi.org/10.1360/sspma2015-00280

Tan, H., & Chen, S. (2017). A hybrid DEM-SPH model for deformable landslide and its generated surge waves. *Advances in Water Resources*, *108*, 256–276. https://doi.org/10.1016/j.advwatres.2017.07.023

Vacondio, R., Mignosa, P., & Pagani, S. (2013). 3D SPH numerical simulation of the wave generated by the Vajont rockslide. *Advances in Water Resources*, *59*, 146–156. https://doi.org/10.1016/j.advwatres.2013.06.009

Viroulet, S., Sauret, A., & Kimmoun, O. (2014). Tsunami generated by a granular collapse down a rough inclined plane. *EPL (Europhysics Letters)*, *105*(3), 34004. https://doi.org/10.1209/0295-5075/105/34004

Viroulet, S., Sauret, A., Kimmoun, O., & Kharif, C. (2013). Granular collapse into water: Toward tsunami landslides. *Journal of Visualization*, *16*(3), 189–191. https://doi.org/10.1007/s12650-013-0171-4

Wang, C., Wang, Y., Peng, C., & Meng, X. (2016). Smoothed particle hydrodynamics simulation of water-soil mixture flows. *Journal of Hydraulic Engineering*, *142*(10), 04010632. https://doi.org/10.1061/(asce)hy.1943-7900.0001163

Wang, S., Hu, J., Huang, C., & Yu, Y. (2021). Graphics processing unit accelerated smoothed particle hydrodynamics—Finite difference method and the application for the flow around a cylinder with forced motions. *Physics of Fluids*, *33*(12), 127122. https://doi.org/10.1063/5.0075262

Wang, X., & Li, J. (2014). Simulation of triaxial response of granular materials by modified DEM. *Science China Physics, Mechanics & Astronomy*, *57*(12), 2297–2308. https://doi.org/10.1007/s11433-014-5605-z

Wang, X., & Li, J. (2017). A new solver for granular avalanche simulation: Indoor experiment verification and field scale case study. *Science China Physics, Mechanics & Astronomy*, *60*(12), 124712. https://doi.org/10.1007/s11433-017-9093-y

Wang, X., Shi, C., Liu, Q., & An, Y. (2021). Numerical study on near-field characteristics of landslide-generated impulse waves in channel reservoirs. *Journal of Hydrology*, *595*, 126012. https://doi.org/10.1016/j.jhydrol.2021.126012

Wang, X., Zhang, Z., & Li, J. (2019). Triaxial behavior of granular material under complex loading path by a new numerical true triaxial engine. *Advanced Powder Technology*, *30*(4), 700–706. https://doi.org/10.1016/j.apt.2018.12.020

Wu, J. (2011). The research and forecasting on the mountain river-type slope surge hazard—A case of Xiaowan reservoir [Master Thesis]. Chengdu University of Technology. (In Chinese).

Xenakis, A. M., Lind, S. J., Stansby, P. K., & Rogers, B. D. (2017). Landslides and tsunamis predicted by incompressible smoothed particle hydrodynamics (SPH) with application to the 1958 Lituya Bay event and idealized experiment. *Proceedings of the Royal Society A: Mathematical, Physical & Engineering Sciences*, *473*(2199), 20160674. https://doi.org/10.1098/rspa.2016.0674

Xu, W. (2020). Fluid-solid coupling method of landslide tsunamis and its application. *Chinese Journal of Rock Mechanics and Engineering*, *39*(7), 1420–1433. (In Chinese). https://doi.org/10.13722/j.cnki.jrme.2020.0061

Yang, X., Liu, M., & Peng, S. (2014). Smoothed particle hydrodynamics modeling of viscous liquid drop without tensile instability. *Computers & Fluids*, *92*, 199–208. https://doi.org/10.1016/j.compfluid.2014.01.002

Yeylaghi, S., Moa, B., Buckham, B., Oshkai, P., Vasquez, J., & Crawford, C. (2017). ISPH modelling of landslide generated waves for rigid and deformable slides in Newtonian and non-Newtonian reservoir fluids. *Advances in Water Resources*, *107*, 212–232. https://doi.org/10.1016/j.advwatres.2017.06.013

Zhan, L., Peng, C., Zhang, B., & Wu, W. (2019). Three-dimensional modeling of granular flow impact on rigid and deformable structures. *Computers and Geotechnics*, *112*, 257–271. https://doi.org/10.1016/j.compgeo.2019.03.019

Zhang, W., Maeda, K., Saito, H., Li, Z., & Huang, Y. (2016). Numerical analysis on seepage failures of dike due to water level-up and rainfall using a water–soil-coupled smoothed particle hydrodynamics model. *Acta Geotechnica*, *11*(6), 1401–1418. https://doi.org/10.1007/s11440-016-0488-y

Zhang, W., Shi, C., An, Y., Yang, S., & Liu, Q. (2018). Viscous elastoplastic SPH model for long-distance high-speed landslide. *International Journal of Computational Methods*, *16*(02), 1846011. https://doi.org/10.1142/s0219876218460118

Zhang, W., Zheng, H., Jiang, F., Wang, Z., & Gao, Y. (2019). Stability analysis of soil slope based on a water-soil-coupled and parallelized smoothed particle hydrodynamics model. *Computers and Geotechnics*, *108*, 212–225. https://doi.org/10.1016/j.compgeo.2018.12.025

Zheng, K., Sun, Z.-C., Sun, J.-W., Zhang, Z.-M., Yang, G.-P., & Zhou, F. (2009). Numerical simulations of water wave dynamics based on SPH methods. *Journal of Hydrodynamics*, *21*(6), 843–850. https://doi.org/10.1016/s1001-6058(08)60221-8

Zhu, C., Huang, Y., & Zhan, L.-T. (2018). SPH-based simulation of flow process of a landslide at Hongao landfill in China. *Natural Hazards*, *93*(3), 1113–1126. https://doi.org/10.1007/s11069-018-3342-8